Unconventional states of bosons with synthetic spin-orbit coupling

Xiangfa Zhou,[1] Yi Li,[2] Zi Cai,[3] and Congjun Wu[2]

[1] *Key Laboratory of Quantum Information, University of Science and Technology of China, CAS, Hefei, Anhui 230026, China*
[2] *Department of Physics, University of California, San Diego, CA 92093, USA*
[3] *Physics Department, Arnold Sommerfeld Center for Theoretical Physics,*
and Center for NanoScience, Ludwig-Maximilians-Universität München, D-80333 München, Germany

Spin-orbit coupling with bosons gives rise to novel properties that are absent in usual bosonic systems. Under very general conditions, the conventional ground state wavefunctions of bosons are constrained by the "no-node" theorem to be positive-definite. In contrast, the linear-dependence of spin-orbit coupling leads to complex-valued condensate wavefunctions beyond this theorem. In this article, we review the study of this class of unconventional Bose-Einstein condensations focusing on their topological properties. Both the 2D Rashba and 3D $\vec{\sigma} \cdot \vec{p}$-type Weyl spin-orbit couplings give rise to Landau-level-like quantization of single-particle levels in the harmonic trap. The interacting condensates develop the half-quantum vortex structure spontaneously breaking time-reversal symmetry and exhibit topological spin textures of the skyrmion type. In particular, the 3D Weyl coupling generates topological defects in the quaternionic phase space as an SU(2) generalization of the usual U(1) vortices. Rotating spin-orbit coupled condensates exhibit rich vortex structures due to the interplay between vorticity and spin texture. In the Mott-insulating states in optical lattices, quantum magnetism is characterized by the Dzyaloshinskii-Moriya type exchange interactions.

PACS numbers:

I. INTRODUCTION

Spin-orbit (SO) coupling plays an important role in interdisciplinary areas of physics. In quantum mechanics, SO coupling arises from the relativistic effect as a low energy approximation to the Dirac equation. Its semi-classic picture is the Thomas precession that electron spin moment couples to a velocity-dependent effective magnetic field generated by the Lorentz transformation of the electric field. In atomic physics, SO coupling constitutes one of the basic elements to the formation of the atomic structures. The development in condensed matter physics shows that SO coupling is indispensable for important phenomena ranging from spintronics[1], anomalous Hall effects[2,3], spin Hall effects[4–7], to topological insulators[8,9]. In particular, topological insulators have become a major research focus of current condensed matter physics.

Most current studies of SO coupling are considered for fermionic systems of electrons. On the other hand, the ultra-cold atomic systems have opened up a whole new opportunity to explore novel states of matter that are not easily accessible in usual condensed matter systems. In particular, it currently becomes experimentally possible to implement various kinds of SO coupled Hamiltonians in ultracold atomic gases for both fermions and bosons[10–16]. The high controllability of these systems makes them an ideal platform to explore novel SO coupled physics with bosons.

An important property of bosons is the "no-node" theorem, which states that in the coordinate representation the many-body ground state wavefunctions are positive-definite[17]. This theorem is valid under very general conditions such as the Laplacian type kinetic energy, arbitrary single-particle potentials, and coordinate-dependent two-body interactions. It applies to most of the known ground states of bosons, including Bose-Einstein condensations (BECs), Mott insulators, and supersolids. Technically, it indicates that the ground state wavefunctions of bosons can be reduced to positive-definite distributions, and thus imposes a strong constraint on bosonic states. For example, it rules out the possibility of time-reversal (TR) symmetry breaking ground states in traditional boson systems. Considerable efforts have been made in exploring unconventional BECs beyond the "no-node" theorem[18]. One way is the meta-stable state of bosons in high orbital bands in optical lattices[19–22], because the "no-node" theorem does not apply to excited states. Unconventional BECs with complex-valued condensate wavefunctions have been experimentally realized[23–25].

The kinetic energies of SO coupled systems are no longer Laplacian but linearly depend on momentum, which invalidates the necessary conditions for the "no-node" theorem as pointed out in Ref. [18]. This provides another way towards unconventional BECs. For instance, the Rashba SO coupled BECs were early investigated for both isotropic[26] and anisotropic cases[27]. In the isotropic case, Rashba coupling leads to degenerate single-particle ground states along a ring in momentum space whose radius k_{so} is proportional to the SO coupling strength. Such a momentum scale is absent in usual BECs in which bosons are condensed to the zero momentum state, and thus bears certain similarities to Fermi momentum in fermion systems. If interaction is spin-independent, the condensates are frustrated in the free space at the Hartree-Fock level, and quantum zero point energy selects a spin-spiral state based on the "order-from-disorder" mechanism. Imposing the trapping potential further quantizes the motion around

the SO ring which leads to Landau level type quantization of the single-particle levels. Under interactions, condensates spontaneously break TR symmetry exhibiting topologically non-trivial spin textures of the skyrmion type[26]. All these features are beyond the framework of "no-node" theorem.

Recently, SO coupled systems with ultra-cold bosons have aroused a great deal of research interest both experimental and theoretical. Experimentally, pioneered by Spielman's group[10–12], BECs with SO coupling in the anisotropic 1D limit have been realized by engineering atom-laser interactions through Raman processes[10–15]. Condensations at finite momenta and exotic spin dynamics have been observed[10–16]. Various experimental schemes have been proposed to realize the isotropic Rashba SO coupling[28–32]. On the side of theory, the Rashba SO coupled bosons have been extensively investigated under various conditions, including the exotic spin structures in the free space, spin textures in harmonic traps, vortex structures in rotating traps, and the SO coupled quantum magnetism in the Mott-insulating states[26,26,27,33–60]. Furthermore, a recent progress shows that a 3D $\vec{\sigma}\cdot\vec{p}$-type SO coupling can also been implemented with atom-laser interactions[44,61]. This is a natural symmetric extension of Rashba SO coupling to 3D dubbed Weyl SO coupling below due to its similarity to the relativistic Hamiltonian of Weyl fermions[62]. The Weyl SO coupled BECs have also been theoretically investigated[44,63–65].

In addition to the ultra-cold atom systems, recent progress in condensed matter systems has also provided an SO coupled boson system of excitons. Excitons are composite objects of conduction electrons and valence holes, both of their effective masses are small, thus relativistic SO coupling exists in the their center of mass motion. The effects of SO coupling on exciton condensations have been theoretically investigated[26,66], including the spin texture formations[26]. An important experiment progress has been achieved in Butov's group[67,68], that spin textures in a cold exciton gas have been observed in GaAs/AlGaAs coupled quantum wells from the photoluminescence measurement.

In the rest of this article, we review the current theoretical progress of studying SO coupled bosons including both the 2D Rashba and 3D Weyl SO couplings. Our emphases will be on the non-trivial topological properties which are absent in conventional BECs. The single-particle spectra will be reviewed in Section II. They exhibit a similar structure to the Landau level quantization in the sense that the dispersion with angular momentum is strongly suppressed by SO couplings[26,36,39,49,61,63,69]. However, a crucial difference from the usual magnetic Landau levels is that these SO coupling induced Landau levels maintain time-reversal symmetry, and thus their topology belongs to the Z_2 class[26]. The interplay between interactions and topology gives rise to a variety of topological non-trivial condensate configurations and spin textures, which will be reviewed in Section III. In particular, the 3D condensates with the Weyl cou-

pling exhibit topological defects in the quaternionic phase space. It is exciting to find an application of the beautiful mathematical concept of quaternions. In Section IV, we review the SO coupled BECs in rotating traps, which are subject to both the Abelian vector potential due to the Coriolis force and the non-Abelian one from SO coupling. The combined effects of the vorticity and spin topology lead to rich structures[70–74], including half quantum vortex lattices, multi-domain of plane-wave states, and giant vortices. Furthermore, in the strongly correlated Mott-insulators, SO coupling effects exhibit in the quantum magnetism as the Dzyaloshinskii-Moriya type exchange interactions[75–79], which will be reviewed in Section V. Conclusions and outlooks are presented in Section VI.

Due to the rapid increasing literatures and the limit of space, we will not cover other important topics, such as SO coupled fermions[16,38,69,80–92], the SO coupled dipolar bosons[46,73]. and the proposals for experimental implementations[28–32].

II. THE SO COUPLED SINGLE-PARTICLE SPECTRA AND THE LANDAU LEVEL QUANTIZATION

We begin with the single-particle properties. Consider the following Hamiltonian of 2D two-component atomic gases with an artificial Rashba SO coupling defined as

$$H_0^{2D,R} = \frac{\vec{p}^2}{2M} + V_{tp}(\vec{r}) - \lambda_R(\sigma_x p_y - \sigma_y p_x), \quad (1)$$

where $\vec{p} = -i\hbar\vec{\nabla}$; the pseudospin components $\uparrow$ and $\downarrow$ refer to two different internal atomic components; λ_R is the Rashba SO coupling strength with the unit of velocity; $V_{tp}(\vec{r}) = \frac{1}{2}M\omega^2 r^2$ is the external trapping potential, and ω is the characteristic frequency of the trap. Another SO coupled Hamiltonian will be considered is the 3D Weyl SO coupling defined as

$$H_0^{3D,W} = \frac{\vec{p}^2}{2M} + V_{tp}(\vec{r}) - \lambda_W \vec{\sigma}\cdot\vec{p}, \quad (2)$$

where λ_W is the SO coupling strength.

Even though we will mostly consider bosons for the Hamiltonians of Eq. 1 and Eq. 2, they possess a Kramer-type TR symmetry $T = i\sigma_y C$ satisfying $T^2 = -1$, where C is the complex conjugate operation. At the single particle level, there is no difference between bosons and fermions. Both Hamiltonians are rotationally invariant but break the inversion symmetry. The 2D Hamiltonian Eq. 1 still possesses the reflection symmetry with respect to any vertical plane passing the center of the trap. For the 3D Hamiltonian Eq. 2, no reflection symmetry exists.

These two typical types of SO interactions have received a lot of attention recently in the community of ultra-cold atoms due to their close connection to condense matter physics. There have already been great experimental efforts on realizing spin-orbit coupling

through atom-light interactions[10–12,14,15,56]. In fact, several proposals for experimental implementations of Eq. 1 and Eq. 2 have appeared in literatures[28,31,32,44,50].

In this section, we review the single-particle properties of Eqs. 1 and 2 focusing on their topological properties. In Sec. II A, their Berry phase structures in momentum space are presented. When the quadratic harmonic trap potential is imposed, the Landau-level type quantization on the energy spectra appears with TR symmetry as shown in Sec. II B. This Landau level quantization provides a clear way to understand novel phases of bosons after turning on interactions. In Sec. II C, wavefunctions of the lowest Landau levels of Eq. 1 and Eq. 2 are explicitly provided. The topology of these Landau level states are reviewed through edge and surface spectra in Sec. II D.

A. Berry connections in momentum space

Both Eq. 1 and Eq. 2 possess non-trivial topology in momentum space. Let us begin with the 2D Rashba Hamiltonian Eq. 1 in the free space, i.e., $V_{tp} = 0$. Its lowest single-particle states in free space is not located at the origin of momentum space but around a ring with the radius $k_{so} = M\lambda_R/\hbar$. The spectra read

$$\epsilon_\pm(\vec{k}) = \frac{\hbar^2}{2M}(k \mp k_{so})^2, \qquad (3)$$

where $\pm$ refer to the helicity eigenvalues of the operator $\vec{\sigma} \cdot (\hat{k} \times \hat{z})$. The corresponding two-component spin wavefunctions of plane-wave states $|\psi_{\vec{k}\pm}\rangle$ are solved as

$$|\psi_{\vec{k}\pm}\rangle = \frac{1}{\sqrt{2}}\begin{pmatrix} e^{-i\frac{\phi_k}{2}} \\ \mp i e^{i\frac{\phi_k}{2}} \end{pmatrix}, \qquad (4)$$

where ϕ_k is the azimuthal angle of $\vec{k}$ in the xy-plane.

For bosons, the lower energy branch states with a fixed helicity are important. The Berry connection $\vec{A}(\vec{k})$ of positive helicity states $\psi_+(\vec{k})$ is defined as

$$\vec{A}(\vec{k}) = \langle\psi_{k+}|i\vec{\nabla}_k|\psi_{k+}\rangle = \frac{1}{2k}\hat{e}_{\phi_k}, \qquad (5)$$

where $\hat{e}_{\phi_k}$ is the unit vector along the azimuthal direction. The Berry curvature F_{ij} is defined as $F_{ij}(\vec{k}) = \partial_{k_i}A_j(\vec{k}) - \partial_{k_j}A_i(\vec{k})$. For a loop winding around the origin $\vec{k} = (0,0)$, the Berry phase is

$$\oint d\vec{k} \cdot \vec{A}(\vec{k}) = \pi. \qquad (6)$$

This is because a two-component spinor after rotating $360°$ does not return to itself but acquires a minus sign. Consequently, $F_{ij}(\vec{k})$ is zero everywhere except contributing a π-flux at the origin of momentum space.

Next we consider the 3D generalization of the Rashba SO coupling of the $\vec{\sigma} \cdot \vec{p}$ type, i.e., the Weyl coupling.

Now in the free space without the trap, the lowest energy single-particle states are located around a sphere in momentum space with the radius also denoted as k_{so} with the value of $k_{so} = M\lambda_W/\hbar$, and the spectra are

$$\epsilon_\pm(\vec{k}) = \frac{\hbar^2}{2M}\left(k \mp k_{so}\right)^2, \qquad (7)$$

where the subscripts $\pm$ refer to the helicity eigenvalues of the operator $\vec{\sigma} \cdot \hat{k}$. The corresponding eigenstates are solved as

$$|\psi_{\vec{k}-}\rangle = \begin{pmatrix} -\sin\frac{\theta_{\vec{k}}}{2} \\ \cos\frac{\theta_{\vec{k}}}{2}e^{i\phi_{\vec{k}}} \end{pmatrix}, \quad |\psi_{\vec{k}+}\rangle = \begin{pmatrix} \cos\frac{\theta_{\vec{k}}}{2} \\ \sin\frac{\theta_{\vec{k}}}{2}e^{i\phi_{\vec{k}}} \end{pmatrix}, \quad (8)$$

where ϕ_k and θ_k are the azimuthal and polar angles of $\vec{k}$ in the spherical coordinates. The Berry connection of the positive helicity states $\psi_{\vec{k},+}$ is

$$\vec{A}(\vec{k}) = \frac{1}{2}\tan\frac{\theta_k}{2}\hat{e}_{\phi_k}, \qquad (9)$$

which is the vector potential for a unit magnetic monopole located at the origin of momentum space, and $\hat{e}_{\phi_k}$ is the azimuthal direction of $\vec{k}$. Defining $B_i = \frac{1}{2}\epsilon_{ijl}F_{jl}$, the corresponding Berry curvature is $\vec{B}(\vec{k}) = \frac{1}{2k^2}\hat{e}_k$, where $\hat{e}_k$ is the radial direction of $\vec{k}$.

B. Landau-level quantization in the harmonic trap from SO couplings

The SO couplings in Eqs. 1 and 2 introduce a SO length scale even in the free space defined as $l_{so} = 1/k_{so}$. The physical meaning of l_{so} is as follows: the low energy states of Eqs. 1 and 2 are not of long-wave length as usual but featured with large magnitude of momentum depending on the SO coupling strength. l_{so} is the length scale of wavepackets that can be formed by using the low energy states on the SO ring of Eq. 1 or the SO sphere of Eq. 2. On the other hand, in the typical experimental setup with ultra-cold quantum gases, a harmonic trap is used to confine atoms. The trapping potential $V(\vec{r}) = \frac{1}{2}m\omega^2 r^2$ introduces another length scale as $l_T = \sqrt{\hbar/(m\omega)}$ as the typical system size. The trap energy scale is $E_{tp} = \hbar\omega$.

It is useful to define a dimensionless parameter $\alpha = l_T/l_{so}$ to describe the relative strength of SO coupling with respect to the trapping potential. Physically, α is the number of wavepackets which can be packed in the trap length. In the limit of large values of α, the trapping potential gives rise to Landau level type quantizations in both 2D and 3D spin-orbit coupling systems[26,50,69,86].

The terminology of Landau levels in this section is generalized from the usual 2D magnetic case as: *topological* single-particle level structures labeled by *angular momentum* quantum numbers with flat or nearly flat spectra. On open boundaries, Landau levels systems develop gapless surface or edge modes which are robust against disorders. We will see that the low energy states of both Eq. 1 and Eq. 2 satisfy this criterion in the case $\alpha \gg 1$.

1. TR invariant Landau levels from the 2D Rashba SO coupling

Let us briefly recall the usual 2D Landau level arising from the magnetic field. In the symmetric gauge with $\vec{A} = \frac{1}{2}B\hat{z} \times \vec{r}$, its Hamiltonian is simply equivalent to a 2D harmonic oscillator in a rotating frame as

$$H_{2D,LL} = \frac{(\vec{p} - \frac{e}{c}\vec{A})^2}{2M} = \frac{p^2}{2M} + \frac{1}{2}M\omega^2 r^2 - \omega L_z, \quad (10)$$

where $L_z = xp_y - yp_x$ and $\omega = \frac{|eB|}{Mc}$. Inside each Landau level, the spectra are degenerate with respect to the magnetic quantum number m. Non-trivial topology of Landau levels comes from the fact that m does not take all the integer values. For example, in the lowest Landau level, m starts from 0 and runs all the positive integer number. This chiral feature is a TR symmetry breaking effect due to the magnetic field.

Next let us consider the 2D Rashba SO coupling of Eq. 1 in the limit of $\alpha \gg 1$. The physics is most clearly illustrated in momentum representation. After projected into the low energy sector of the positive helicity states, the harmonic potential in momentum space becomes a Laplacian subjected to the Berry connection as

$$V_{tp}(\nabla_k) = \frac{M}{2}\omega^2(i\nabla_{\vec{k}} - \vec{A}_{\vec{k}})^2, \quad (11)$$

where $\vec{A}$ is given in Eq. 5 with a π-flux at the origin of the 2D k_x-k_y plane. In momentum space, the trapping potential quantizes the motion on the low energy spin-orbit ring with radius k_{so}, and is mapped to a planar rotor problem. The moment of inertial in momentum space is $I_k = k_{so}^2 M_k$ where M_k is the mass in momentum space defined as $M_k = 1/(M\omega^2)$, and the angular dispersion of energy is $E_{agl}(j_z) = \hbar^2 j_z^2/2I_k = \frac{1}{2\alpha^2}j_z^2 E_{tp}$. Due to the π-flux phase at $\vec{k} = (0,0)$, j_z is quantized to half-integer values. On the other hand, the radial component of the trapping potential in momentum space is just the kinetic energy for the positive helicity states

$$H_K = \frac{1}{2}M_k\omega^2(k - k_{so})^2. \quad (12)$$

For states near the low energy spin-orbit ring, the radial motion can be approximated as 1D harmonic oscillations, and the energy gap remains as $\hbar\omega$. Combining the radial and angular dispersions together, we arrive at

$$E_{n_r,j_z} \approx \left\{n_r + \frac{j_z^2}{2\alpha^2} + \frac{1}{2}(1 - \alpha^2)\right\}E_{tp}, \quad (13)$$

where n_r is the radial quantum number, and $\frac{1}{2}(1 - \alpha^2)$ is the constant of zero point energy.

The degeneracy over angular momentum quantum numbers is a main feature of Landau level quantization. For the Hamiltonian Eq. 1, although its spectra Eq. 13 are not exactly flat with respect to j_z, they are strongly

suppressed at $\alpha \gg 1$, thus these low energy levels are viewed as Landau levels. The radial quantum number n_r serves as the Landau level index and the gaps between Landau levels are roughly E_{tp}. For states in the n_r-th Landau level with $|j_z| \le \sqrt{2}\alpha$, their energies remain lower than the bottom of the next Landau level, thus they can be viewed as gapped bulk states. Actually, the similarities of these SO coupled states to Landau levels are more than just spectra flatness but their non-trivial topology will be explained in Sec. II D.

2. 3D Landau levels from the Weyl SO coupling

The 3D Landau level systems are not as well-known as the 2D case of Eq. 10. Recently, a large progress has been made in generalizing Eq. 10 to 3D with exactly flat energy dispersions[38,93]. In particular, they can be constructed with the full 3D rotation symmetry by coupling spin-$\frac{1}{2}$ fermions with the SU(2) gauge potential. The Hamiltonian is equivalent to a 3D harmonic oscillator plus SO coupling as

$$H_{3D,LL} = \frac{p^2}{2M} + \frac{1}{2}M\omega^2 r^2 - \omega\vec{L}\cdot\vec{\sigma}. \quad (14)$$

Excitingly, the lowest Landau level wavefunctions of Eq. 14 possess elegant analytic properties, satisfying the Cauchy-Riemann-Fueter condition of quaternionic analyticity. Just like that the complex analyticity is essential for the construction of fractional quantum Hall Laughlin states, the quaternionic analyticity is expected to play an important role in high dimensional fractional topological states. These 3D Landau level states preserve both TR and parity symmetry. The 3D Landau levels have also been generalized to the relativistic Dirac particles[94].

Now let us come back to the Hamiltonian of Eq. 2 with the 3D Weyl SO coupling and a trap potential. The parallel analysis to the 2D Rashba case applies. Again, in the limit of $\alpha \gg 1$, after the projection into the sector of the positive helicity states, the trap potential becomes $V_{tp}(\nabla_k) = \frac{1}{2}M(i\vec{\nabla}_k - \vec{A}_k)^2$ and $\vec{A}_k$ takes the form of a magnetic monopole one in Eq. 9. The problem is reduced to a spherical rotor problem in momentum space on the low energy SO sphere with the radius k_{so}. The monopole structure of the Berry connection quantizes the total angular momentum j to half-integer values. Similarly to the 2D Rashba case, the low energy spectra are approximated as

$$E_{n_r,j,j_z} \approx \left\{n_r + \frac{j(j+1)}{2\alpha^2} + \frac{1}{2}(1 - \alpha^2)\right\}E_{tp}. \quad (15)$$

Again the angular dispersion is strongly suppressed by SO coupling at $\alpha \gg 1$. These spectra exhibit quasi-degeneracy over the 3D angular momentum good quantum numbers of j and j_z, and thus can be viewed as a 3D Landau level quantization with TR symmetry. The length scale of these Landau level states is also the SO

length l_{so}. Topological properties of these Landau level states will be studied in Sec. II D.

C. Lowest Landau level wavefunctions and parent Hamiltonians

The Landau level energy spectra of Eq. 13 in 2D and Eq. 15 in 3D are not exactly flat but with weak dispersions over angular momentum quantum numbers. Nevertheless, parent Hamiltonians based on slight modification on Eqs. 1 and 2 can be constructed. Their lowest Landau level spectra are exactly flat and their wavefunctions can be solved analytically as shown in Eqs. 17 and 19 below. These wavefunctions maintain TR symmetry but break parity. In the limit of $\alpha \gg 1$ and for Landau level states with angular momenta $|j_z| < \alpha$ in 2D or $j < \alpha$ in 3D, the lowest Landau level wavefunctions of Eqs. 1 and 2 are well approximated by these expressions.

For the 2D case, the parent Hamiltonian is just

$$H_0^{2D,P} = H_0^{2D,R} - \omega L_z \sigma_z, \qquad (16)$$

where $L_z = xp_y - yp_x$ and the coefficient ω is the same as the trap frequency. As shown in Ref. [61], its lowest Landau level wavefunctions are solved as

$$\psi_{2D,j_z}^{LLL}(r,\phi) = e^{-\frac{r^2}{2l_T^2}} \begin{pmatrix} e^{im\phi} J_m(k_{so}r) \\ -e^{i(m+1)\phi} J_{m+1}(k_{so}r) \end{pmatrix}, \quad (17)$$

where ϕ is the azimuthal angle; $j_z = m + \frac{1}{2}$; J_m is the m-th order Bessel function. The lowest Landau level energy is exactly flat as $E^{LLL} = (1 - \frac{\alpha^2}{2})\hbar\omega$.

In the case of $\alpha \gg 1$ and for small values of $|j_z| \approx m < \alpha$, the decay of the wavefunctions Eq. 17 is controlled by the Bessel functions rather than the Gaussian factor. Their classic orbit radiuses scale as $\rho_{c,j_z} \approx ml_{so}$. Since L_z linearly depends on ρ, the effect of the $L_z\sigma_z$ term compared to that of the Rashba one is at the order of $\rho_{c,j_z}\omega/\lambda_R \approx m/\alpha^2 \ll 1$. Thus Eq. 16 is simply reduced to Eq. 1 whose lowest Landau level wavefunctions are well approximated by Eq. 17. In this case, the length scale of Landau level states is determined by the SO length l_{so} instead of the trap length l_T. The reason is that these Landau levels are composed from plane-wave states with a fixed helicity on the low energy Rashba ring. The confining trap further opens the gap at the order of $\hbar\omega$ between SO coupled Landau levels.

On the contrary, in the opposite limit, i.e., $|j_z| \approx m \gg \alpha^2$, the $L_z\sigma_z$ term dominates and the Rashba term can be neglected. In this case, Eq. 16 is reduced into $p^2/2M + \frac{1}{2}M\omega^2 r^2 - \omega L_z \sigma_z$ with σ_z conserved. In each spin eigen-sector, it is just the usual Landau level Hamiltonian in the symmetric gauge with opposite chiralities for spin up and down, respectively. Nevertheless, at $m \gg \alpha^2$, the approximation of the projection into the Rashba ring for Eq. 1 is not valid, and the eigenstates are no longer Landau levels. For the intermediate values

of $\alpha < |j_z| < \alpha^2$, the physics is a crossover between the above two limits.

Following the same logic, the 3D parent Hamiltonian with exactly flat SO coupled Landau levels is

$$H_0^{3D,P} = H_0^{3D,W} - \omega \vec{L} \cdot \vec{\sigma}, \qquad (18)$$

where $\vec{L} = \vec{r} \times \vec{p}$ is the 3D orbital angular momentum, and the coefficient of the $\vec{L} \cdot \vec{\sigma}$ term is the same as the trap frequency. Again, as shown in Ref. [61], the lowest Landau level wavefunctions of Eq. 18 are solved analytically as

$$\psi_{3D,jj_z}^{LLL}(\vec{r}) = e^{-\frac{r^2}{2l_T^2}} \Big\{ j_l(k_{so}r)Y_{+,j,l,j_z}(\Omega_r) + ij_{l+1}(k_{so}r) \\ \times \ Y_{-,j,l+1,j_z}(\Omega_r) \Big\}, \qquad (19)$$

where j_l is the l-th order spherical Bessel function; $Y_{\pm,j,l,j_z}$'s are the SO coupled spherical harmonics with total angular momentum quantum numbers $j = l \pm \frac{1}{2}$ and j_z, which are composed of the spherical harmonics Y_{lm} and spin-$\frac{1}{2}$ spinors. These lowest Landau level states are degenerate over all the values of (jj_z) with $E^{LLL} = (\frac{3}{2} - \frac{\alpha^2}{2})\hbar\omega$.

Following the same reasoning as in the 2D case, in the limit of $\alpha \gg 1$, we can divide the lowest Landau level states of Eq. 19 into three regimes as $j < \alpha$, $j \gg \alpha^2$, and $\alpha < j < \alpha^2$, respectively. At $j < \alpha$, the classic orbit radius scales as $r_{c,j}/l_T \approx \frac{j}{\alpha}$, and thus $\vec{\sigma} \cdot \vec{L}$ comparing with $\vec{\sigma} \cdot \vec{p}$ is a perturbation at the order of $j/\alpha^2 \ll 1$. In this regime, the lowest Landau level wavefunctions of Eq. 2 are well approximated by Eq. 19. On the contrary, in the regime of $j \gg \alpha^2$, $\vec{\sigma} \cdot \vec{L}$ dominates over $\vec{\sigma} \cdot \vec{p}$, thus the eigenstates of Eqs. 18 and 2 are qualitatively different. In this case, Eq. 18 is reduced to the 3D Landau level Hamiltonian Eq. 14.

D. The Z_2-stability of helical edge and surface states

Non-trivial topology of the 2D Landau level manifests from the appearance of robust gapless edge states. The classic radius r_c of each Landau level state expands as m increases. For example, in the lowest Landau level, $r_c = \sqrt{m}l_B$ where $l_B = \sqrt{\frac{\hbar c}{|eB|}}$ is the cyclotron radius. With an open boundary, as m becomes large enough, states are pushed to the boundary[95]. Unlike the flat bulk spectra, the edge spectra are dispersive, always increasing with m, and thus are chiral and robust against external perturbations. Each Landau level contributes one branch of chiral edge modes. If the system is filled with fermions, when chemical potential μ lies in the gap between Landau levels, the chiral edge states give rise to the quantized charge transport.

For Landau levels of the Rashba SO coupling in Eq. 1, a marked difference is that these states are TR invariant. The angular momentum j_z in Eq. 13 takes all the

half-integer values as $j_z = \pm\frac{1}{2}, \pm\frac{3}{2}, ..., \pm(m+\frac{1}{2}), ...$, and thus these states are helical instead of chiral. Since the system described by Eq. 1 does not possess translation symmetry, the usual method of calculating topological index based on lattice Bloch wave structures in Brillouin zones does not work.

Nevertheless, the non-trivial topology should exhibit on the robustness of edge states. The trap length l_T can be used as the sample size by imposing an open boundary condition at $r = l_T$. States with $|j_z| < \alpha$ are bulk states localized within the region of $r < l_T$. States with $|j_z| \sim \alpha$ are pushed to the boundary, whose spectra disperse to high energy rapidly. For a given energy E lying between Landau level gaps, each Landau level with bulk energy blow E contributes to a pair of degenerate edge modes $\psi_{\pm j_z}$ due to TR symmetry. Nevertheless, these two edge modes are Kramer doublets under the TR transformation satisfying $T^2 = -1$. The celebrated Kane-Mele Z_2 argument for translational invariant systems can be generalized to these rotation invariant systems by replacing linear momentum with the angular momentum. If a given energy cuts odd numbers of helical edge modes, then any TR invariant perturbation cannot mix these modes to open a gap. Consequently, the topological nature of such a system is characterized by the Z_2 index. The effective edge Hamiltonian can be derived as in the plane-wave basis if the edge is considered locally flat

$$H_{edge} = v\Big(\sin\eta(\vec{p}\times\hat{n})\cdot\sigma_z + \cos\eta[(\vec{p}\times\hat{n})\cdot\hat{z}](\vec{\sigma}\cdot\hat{n})\Big),$$
(20)

where $\hat{n}$ is the local normal direction on the circular edge in the 2D plane; v is the linearized velocity of the edge modes; η is a parameter angle depending on the details of the systems. Both terms are allowed by rotation symmetry, TR symmetry, and the vertical mirror symmetry in this system. Each edge channel is a branch of helical one-dimensional Dirac fermion modes.

Parallel analysis can be applied to the surface state of the 3D Hamiltonian Eq. 2. Again, due to the TR symmetry, the surface state is helical instead of chiral. Its topological class also belongs to Z_2. If the surface is sufficiently large, and thus can be locally taken as flat, we can construct the surface Dirac Hamiltonian by using plane-wave basis based on the symmetry analysis as

$$H_{sfc} = v\Big\{\sin\eta(\vec{p}\times\vec{\sigma})\cdot\hat{n} + \cos\eta\big[\vec{p}\cdot\vec{\sigma} - (\vec{p}\cdot\hat{n})(\vec{\sigma}\cdot\hat{n})\big]\Big\},$$
(21)

where $\hat{n}$ is the local normal direction to the 2D surface. Due to the local $SO(2)$ rotational symmetry around $\hat{n}$, the in-plane momentum p_x and p_y cannot couple to σ_z, thus spin has to lie in the xy-plane. The first Rashba term favors spin and momentum with a relative angle of $90°$, while the second favors spin aligning with momentum. For a general value of η depending on non-universal surface properties, Eq. 21 determines a relative rotation between spin and momentum orientation at the angle of η.

III. TOPOLOGICAL SPIN TEXTURES AND THE QUATERNIONIC PHASE DEFECTS IN A HARMONIC TRAP

In this section, we review the unconventional BECs with interactions and SO couplings, including both Rashba and the 3D Weyl types, in the harmonic trap. The 2D Rashba case is presented in Sec. III A. The linear dependence on momentum of SO coupling invalidates the proof of "no-node" theorem. Consequently, a general feature of SO coupled BECs is the complex-valued condensate wavefunctions and the spontaneous TR symmetry breaking. For the Rashba case, the skyrmion type spin textures and half-quantum vortex were predicted in the harmonic trap[26]. Furthermore, due to the Landau level structures of single-particle states, rich patterns of spin textures have been extensively investigated in literatures[26,39,49]. A nice introduction of topological defects in the ultra-cold atom context can be found in Ref. [96]. Recently, exact diagonalization work has further showed evidence of strongly correlated phase with non-trivial topology[97].

Even more interesting physics shows in 3D Weyl SO coupling, which will be reviewed in Sec. III C. The non-trivial topology of the condensate wavefunction is most clearly expressed in the quaternionic representation[64,94]. Quaternions are a natural extension of complex numbers as the first discovered non-commutative division algebra, which has been widely applied in quantum physics[98–100]. The condensation wavefunctions exhibit defects in the quaternionic phase space as the 3D skyrmions, and the corresponding spin density distributions are characterized by non-zero Hopf invariants.

A. Half-quantum vortices and spin texture skyrmions with Rashba SO coupling

Let us consider a 3D two-component boson system with contact spin-independent interactions and with Rashba SO coupling in the xy-plane. Since the Rashba SO coupling is 2D, interesting spin textures only distribute in the xy-plane. For simplicity, the condensate is set uniform along the z-direction, then the problem is reduced to a 2D Gross-Pitaevskii (GP) equation as

$$\Big\{-\frac{\hbar^2\nabla^2}{2M} + i\hbar\lambda_R(\nabla_x\sigma_{y,\alpha\beta} - \nabla_y\sigma_{x,\alpha\beta}) + gn(r,\phi)$$
$$+ \frac{1}{2}M\omega^2 r^2\Big\}\psi_\beta(r,\phi) = E\psi_\alpha(r,\phi),$$
(22)

where ψ_α's with the subscript $\alpha =\uparrow,\downarrow$ are two-component condensate wavefunctions; $n(r,\phi)$ is the particle density; g describes the s-wave scattering interaction. The interaction energy scale is defined as $E_{int} = gN_0/(\pi l_T^2 L_z)$, where L_z is the system size along the z-axis, and the dimensionless interaction parameter is defined as $\beta = E_{int}/(\hbar\omega_T)$.
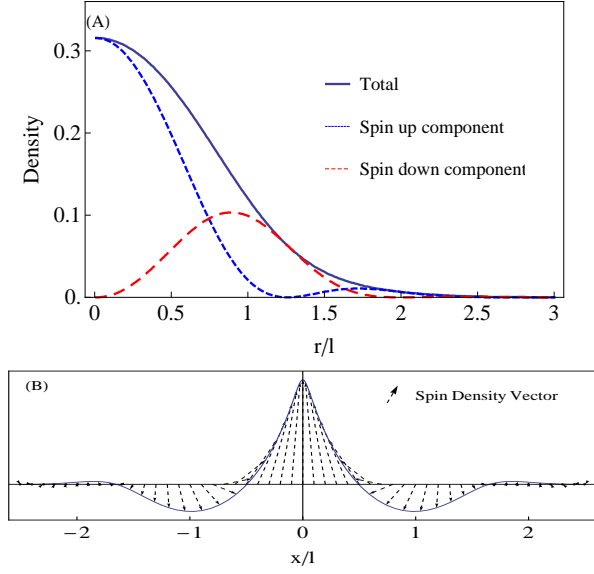
FIG. 1: (A) The radial density distribution of spin up and down components, and the total density distribution in the unit of $N_0 = \int d^3\vec{r}\{|\psi_\uparrow(\vec{r})|^2 + |\psi_\downarrow(\vec{r})|^2\}$ at $\alpha = 2$ and $\beta = 5$. (B) The skyrmion type spin texture configuration is plotted in the xz-plane. From Refs. 26.

We start with weak SO coupling, $\alpha \sim 1$, and with weak interactions. In this case, the energy of single-particle ground state with $j_z = \pm\frac{1}{2}$ is well separated from other states. If interactions are not strong enough to mix the ground level with other levels, the condensate wavefunction remains the same symmetry structure carrying $j_z = \frac{1}{2}$, or, $-\frac{1}{2}$, thus bosons condense into one of the TR doublets,

$$\psi_{\frac{1}{2}}(r,\phi) = \begin{pmatrix} f(r) \\ g(r)e^{i\phi} \end{pmatrix}, \quad \psi_{-\frac{1}{2}}(r,\phi) = \begin{pmatrix} -g(r)e^{-i\phi} \\ f(r) \end{pmatrix}, \tag{23}$$

where $f(r)$ and $g(r)$ are real radial functions. In the non-interacting limit, $f(r) \approx J_0(k_0 r)e^{-\frac{r^2}{4l_T^2}}$ and $g(r) \approx J_1(k_0 r)e^{-\frac{r^2}{4l_T^2}}$ as shown in Eq. 17. Repulsive interactions expand the spatial distributions of $f(r)$ and $g(r)$, but the qualitative picture remains. Therefore, one spin component stays in the s-state and the other in the p-state. This is a half-quantum vortex configuration which spontaneously breaks TR symmetry[26].

One possibility is that the condensate wavefunction may take linear superpositions of the Kramer doublet in Eq. 23. The superposition principle usually does not apply due to the non-linearity of the GP equation. Nevertheless, if the interaction of the GP equation is spin-independent, all the linear superpositions of the Kramer doublet in Eq. 23 are indeed degenerate. This is an accidental degeneracy at the mean-field level which is not protected. Quantum fluctuations remove this degeneracy as shown in the exact diagonalization calculation in

Ref. 49 and select either one of $\psi_{\pm\frac{1}{2}}$. In other words, quantum fluctuations can induce a spin-dependent interaction beyond the mean-field level[26]. Certainly, we can also prepare the initial state with the average j_z per particle $\pm\frac{1}{2}$, say, by cooling down from the fully polarized spin up or down state, then $\psi_{\pm\frac{1}{2}}$ will be reached. On the other hand, if an additional spin-dependent interaction is introduced,

$$H'_{int} = g' \int d^3\vec{r}\Big(n_\uparrow(r) - n_\downarrow(r)\Big)^2, \tag{24}$$

then even the mean-field level degeneracy is removed. In this case, as shown in Ref. [51], the condensate wavefunctions of $\psi_{\pm\frac{1}{2}}$ will also be selected.

The spin distribution of a condensate wavefunction is expressed as

$$\vec{S}(r,\phi) = \psi_\alpha^*(r,\phi)\vec{\sigma}_{\alpha\beta}\psi_\beta(r,\phi), \tag{25}$$

which is known as the 1st Hopf map. Without loss of generality, the condensate of $\psi_{\frac{1}{2}}$ is considered, and its $\vec{S}(\vec{r})$ is expressed as

$$S_x(r,\phi) = \rho\sin 2\gamma(r)\cos\phi, \quad S_y(r,\phi) = \rho\sin 2\gamma(r)\sin\phi,$$
$$S_z(r,\phi) = \rho\cos 2\gamma(r), \tag{26}$$

where $\rho(r) = \sqrt{|f(r)|^2 + |g(r)|^2}$, and the parameter angle $\gamma(r)$ is defined through

$$\cos\gamma(r) = \frac{f(r)}{\rho(r)}, \quad \sin\gamma(r) = \frac{g(r)}{\rho(r)}. \tag{27}$$

Since the Fourier components of $f(r)$ and $g(r)$ are located around the Rashba ring in momentum space, they oscillate along the radial direction with an approximated pitch value of k_0 as shown in Fig. 1 (A). Because $f(r)$ and $g(r)$ are of the s and p-partial waves, respectively, they are with a relative phase shift of $\frac{\pi}{2}$. At $r = 0$, $f(r)$ is at maximum and $g(r)$ is 0. As r increases, roughly speaking, the zero points of $f(r)$ corresponds to the extrema of $g(r)$ and vice versa, thus $\gamma(r)$ spirals as r increases. At the n-th zero of $g(r)$ denoted r_n, $\gamma(r_n) = n\pi$ ($n \geq 0$ and we define $r_0 = 0$).

Consequently, $\vec{S}$ spirals in the zx-plane along the x-axis as shown in Fig. 1 B. The entire distribution of $\vec{S}$ can be obtained through a rotation around the z-axis. This is a skyrmion configuration which is a non-singular topological defect mapping from the real space R^2 to the spin orientation space of the S^2 sphere. If the coordinate space is a closed manifold S^2, this mapping is characterized by the integer valued Pontryagin index $\pi_2(S^2) = Z$, or, the winding number. However, the coordinate space is the open R^2, and $\rho(r)$ decays exponentially at large distance $r \gg l_T$, thus the rigorously speaking the covering number is not well-defined. Nevertheless, in each concentric circle $r_n < r < r_{n+1}$, $\gamma(r)$ varies from $n\pi$ to $(n+1)\pi$, which contributes to the winding number by 1.
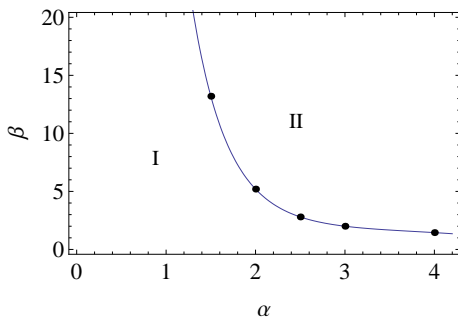
FIG. 2: The phase boundary of β_c v.s α between (I) the skyrmion condensates with $j_z = \pm\frac{1}{2}$ and (II) rotational symmetry breaking condensates. From Ref. 26.

If we use the trap length scale l_T as the system size, the winding number is roughly at the order of α.

The radial oscillation of the spin density is in analogy to the Friedel oscillations in Fermi systems. Around an impurity in electronic systems, the screening charge distribution exhibits the radial oscillation on top of the enveloping exponential decay. The oscillation pitch is $2k_f$ reflecting the discontinuity of the Fermi distribution on the spherical Fermi surface. Different from the usual boson systems, the SO coupled ones have a low energy ring structure in momentum space in analogous to the Fermi surface, thus in real space spin density also oscillates in the presence of spatial inhomogeneity.

In the regime of intermediate SO coupling strength, the level spacing between single particle states within the same Landau level is suppressed as shown in Eq. 13. In the case that interactions are strong enough to mix energy levels with different angular momenta in the same lowest Landau level but not among different Landau levels, condensates do not keep rotation symmetry any more. The calculated phase boundary of interaction strength β v.s. SO coupling strength α is plotted in Fig. 2. In this regime, the distributions are no long concentric but split into multi-centers and finally form a triangular skyrmion lattice structure as calculated in Refs. [49], [39]. This 2D skyrmion lattice structure is a characteristic feature brought by SO coupling.

B. Plane-wave type condensations with Rashba SO coupling

If interactions are strong enough to mix states in different Landau levels, then the influence of the confining trap is negligible. The condensate configurations in the free space was calculated beyond the mean-field GP equation level in Ref. [26]. Bosons select the superposition of a pair of states with opposite momenta $\vec{k}$ and $-\vec{k}$ on the low energy Rashba ring to condense. These spin eigenstates of these two states are orthogonal, thus the condensate can avoid the positive exchange interactions. As is well known, avoiding exchange energy is the main driving force towards BEC. For spin-independent interactions, the condensate wavefunctions exhibit degeneracy at the Hartree-Fock level regardless of the relative weight between these two plane-wave components. This is a phenomenon of "frustration". Quantum zero-point energy from the Bogoliubov quasi-particle spectra selects an equal weight supposition through the "order-from-disorder" mechanism. Such a condensate exhibits spin-spiral configuration.

Various literatures have also studied the case of spin-dependent interactions in which the Hartree-Fock theory is already enough to select either the spin-spiral state, or, a ferromagnetic condensate with a single plane-wave component[33,34].

C. Quaternionic phase defects of the 3D Weyl SO coupling

Next we review the condensates with the 3D Weyl SO coupling in the harmonic trap. The corresponding GP equation is very similar to Eq. 22 of the Rashba case. Only slight modifications are needed by replacing the spatial dimension 2 with 3, and by replacing the Rashba term with $-i\hbar\lambda_W \vec{\nabla} \cdot \vec{\sigma}$. Amazingly, in this case condensate wavefunctions exhibit topological structures in the quaternionic representation[63].

1. The quaternionic representation

Just like a pair of real numbers form a complex number, the two-component spinor $\psi = (\psi_\uparrow, \psi_\downarrow)^T$ is mapped to a single quaternion following the rule

$$\xi = \xi_0 + \xi_1 i + \xi_2 j + \xi_3 k, \qquad (28)$$

where $\xi_0 = \text{Re}\psi_\uparrow, \xi_1 = \text{Im}\psi_\downarrow, \xi_2 = -\text{Re}\psi_\downarrow, \xi_3 = \text{Im}\psi_\uparrow$. i, j, k are the imaginary units satisfying $i^2 = j^2 = k^2 = ijk = -1$, and the anti-commutation relation $ij = -ji = k$. Quaternion can also be expressed in the exponential form as

$$\xi = |\xi|e^{\omega\gamma} = |\xi|(\cos\gamma + \omega\sin\gamma), \qquad (29)$$

where $|\xi| = \sqrt{\xi_0^2 + |\vec{\xi}|^2}$ and $|\vec{\xi}|^2 = \xi_1^2 + \xi_2^2 + \xi_3^2$; ω is the unit imaginary unit defined as $\omega = (\xi_1 i + \xi_2 j + \xi_3 k)/|\vec{\xi}|$ which satisfies $\omega^2 = -1$; the argument angle γ is defined as $\cos\gamma = \xi_0/|\xi|$ and $\sin\gamma = |\vec{\xi}|/|\xi|$.

Similarly to the complex phase $e^{i\phi}$ which spans a unit circle, the quaternionic phases $e^{\omega\gamma}$ span a unit three dimensional sphere S^3. The spin orientations lie in the S^2 Bloch sphere. For a quaternionic wavefunction, its corresponding spin distribution is defined through the 1st Hopf map defined in Eq. 25 as a mapping $S^3 \to S^2$. Due to the homotopy groups[101,102] $\pi_3(S^3) = Z$ and $\pi_3(S^2) = Z$, both quaternionic condensate wavefunctions and spin distributions can be non-trivial. The winding
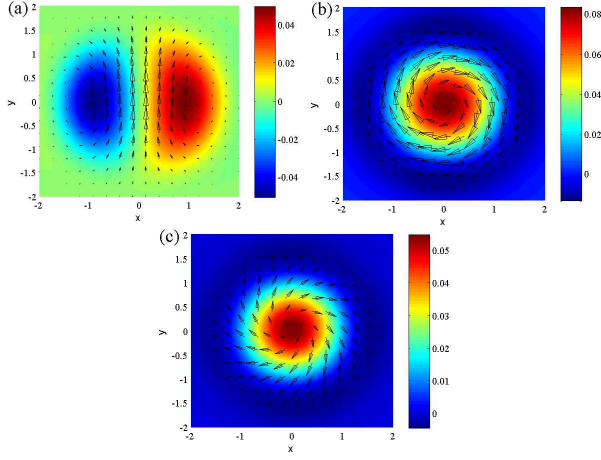
FIG. 3: The distribution of $\vec{S}(\vec{r})$ in a) the xz-plane and in the horizontal planes with b) $z=0$ and c) $z/l_T = \frac{1}{2}$ with $\alpha = 1.5$, $c=1$, and $\beta = 30$. The color scale shows the magnitude of out-plane component S_y in a) and S_z in b) and c). The 3D distribution of $\vec{S}(\vec{r})$ is topologically non-trivial with a non-zero Hopf invariant. The length unit in all the figures is l_T. From Ref. 63.
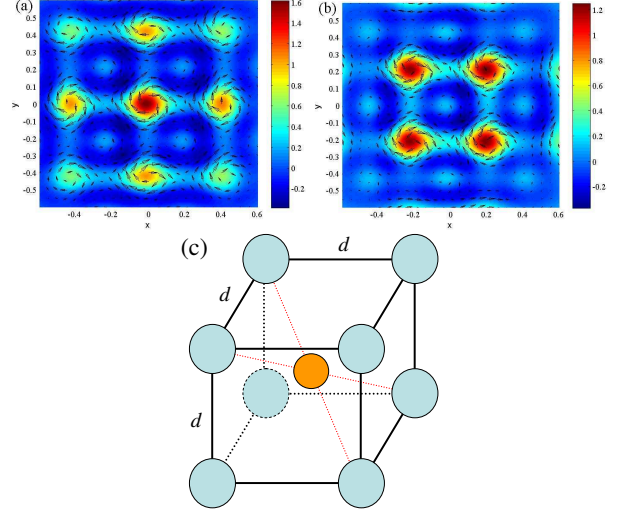

FIG. 4: The distribution of $\vec{S}(\vec{r})$ for parameter values $\alpha = 15$, $\beta = 0.8$, and $c = 1$ in horizontal cross-sections with (a) $z/l_T = 0$, (b) $z/l_T = 0.2$, respectively. The spin texture lattice exhibits a bcc configuration as sketched in (c). The color scale shows the value of S_z in (a) and (b). From Ref. 63.

number of $S^3 \to S^3$ is the 3D skyrmion number, and that of the $S^3 \to S^2$ is the Hopf invariant, both are integer-valued.

Let us apply the above analysis to the lowest single-particle level with $j_z = j = \frac{1}{2}$

$$\psi_{j=j_z=\frac{1}{2}}(r,\hat{\Omega}) = f(r)Y_{+,\frac{1}{2},0,\frac{1}{2}}(\hat{\Omega}) + ig(r)Y_{-,\frac{1}{2},1,\frac{1}{2}}(\hat{\Omega}),$$
(30)

where $Y_{+,\frac{1}{2},0,\frac{1}{2}}(\hat{\Omega}) = (1,0)^T$ and $Y_{-,\frac{1}{2},1,\frac{1}{2}}(\hat{\Omega}) = (\cos\theta, \sin\theta e^{i\phi})^T$. As shown in Eq. 19, in the non-interacting limit, $f(r) \approx j_0(k_0 r)e^{-\frac{r^2}{4l_T^2}}$ and $g(r) \approx j_1(k_0 r)e^{-\frac{r^2}{4l_T^2}}$. The corresponding quaternionic expression is

$$\xi_{j=j_z=\frac{1}{2}}(r,\hat{\Omega}) = \rho(r)e^{\omega(\hat{\Omega})\gamma(r)},$$
(31)

where $\rho(r)$ and $\gamma(r)$ are defined in the same way as the 2D case in Eq. 26; the imaginary unit,

$$\omega(\hat{\Omega}) = \sin\theta\cos\phi\, i + \sin\theta\sin\phi\, j + \cos\theta\, k,$$
(32)

is along the direction of $\hat{\Omega}$.

2. Quaternionic phase defects and spin textures with non-zero Hopf invariants

The analysis on the topology of the Weyl condensates can be performed in parallel to the above 2D Rashba case. Again in the case of weak SO coupling, interactions only expand the spatial distribution of $f(r)$ and $g(r)$ in Eq. 30

from their non-interacting forms. The radial wavefunction $f(r)$ and $g(r)$ follow the same oscillating pattern as those in the Rashba case, thus so does the parameter angle $\gamma(r)$ which starts from 0 at the origin and reaches $n\pi$ at the n-th zero of $f(r_n) = 0$. For the quaternionic phase $e^{\omega(\hat{\Omega})\gamma(r)}$, its imaginary unit $\omega(\hat{\Omega})$ is of one-to-one correspondence to every direction in 3D, thus it exhibits a non-trivial mapping from the 3D coordinate space R^3 to S^3, which is known as a 3D skyrmion configuration.

For a closed 3-manifold, the Pontryagin index of winding number is $\pi_3(S^3) = Z$, i.e., integer. Again here the real space is open. In each concentric spherical shell with $r_n < r < r_{n+1}$ whose thickness is at the scale of l_{so}, $\gamma(r)$ spirals from $n\pi$ to $(n+1)\pi$, thus this shell contributes 1 to the winding number from real space to the quaternionic phase manifold. If the system size is truncated at the trap length l_T, again the winding number is approximately α. In comparison, in the 2D Rashba case reviewed in Sec. III A, $\vec{S}(\vec{r})$ exhibits the 2D skyrmion configuration[26,39,49], but condensation wavefunctions have no well-defined topology due to the fact that $\pi_2(S^3) = 0$.

A comparison can be made with the $U(1)$ vortex in the single-component BEC. In 2D, it is a topological defect with a singular core. Moving around the circle enclosing the core, the phase winds from 0 to 2π, and thus the winding number is 1. The above 3D skyrmion phase defect is a natural generalization to the two-component case whose phase space is S^3 in the quaternionic representation and is isomorphic to the $SU(2)$ group manifold. These 3D skyrmions are non-singular defects similar to a 1D ring of rotating BEC which carries a non-zero phase winding number but the vortex core lies outside the ring.

The non-trivial topology of the condensate wavefunctions leads to a topologically non-trivial distribution of spin density $\vec{S}(\vec{r})$. The 1st Hopf map defined in Eq. 25 becomes very elegant in the quaternionic representation as

$$S_x i + S_y j + S_z k = \frac{1}{2}\bar{\xi}k\xi, \qquad (33)$$

where $\bar{\xi} = \xi_0 - \xi_1 i - \xi_2 j - \xi_3 k$ is the quaternionic conjugate of ξ. For the condensate wavefunction Eq. 31, $\vec{S}(\vec{r})$ is calculated as

$$\begin{bmatrix} S_x(\vec{r}) \\ S_y(\vec{r}) \end{bmatrix} = g(r)\sin\theta \begin{bmatrix} \cos\phi & -\sin\phi \\ \sin\phi & \cos\phi \end{bmatrix} \begin{bmatrix} g(r)\cos\theta \\ f(r) \end{bmatrix},$$
$$S_z(\vec{r}) = f^2(r) + g^2(r)\cos 2\theta, \qquad (34)$$

which exhibits a perfect axial symmetry around the z-axis. $\vec{S}(\vec{r})$ is plotted in Fig. 3 at different cross sections. In the xy-plane, it exhibits a 2D skyrmion pattern, whose in-plane components are along the tangential direction. As the horizontal cross-section shifted along the z-axis, $\vec{S}(\vec{r})$ remains the 2D skyrmion-like, but its in-plane components are twisted around the z-axis. According to the sign of the interception z_0, the twist is clockwise or anti-clockwise, respectively. This 3D distribution pattern of $\vec{S}(\vec{r})$ is characterized by an integer valued Hopf invariant characterized by $\pi_3(S^2) = Z$.

As SO coupling strength increases, condensates break rotational symmetry by mixing different states with different values of j in the lowest Landau level. In particular, in the case of $\alpha \gg 1$, a 3D lattice structure of topological defects is formed as shown in Fig. 4. Each site is a single skyrmion for the condensate wavefunction $\xi(\vec{r})$, whose spin distribution is a texture with approximately a unit Hopf invariant. Spin textures form a square lattice in the xy-plane with the lattice constant $d \simeq 2\pi l_{so} = 2\pi l_T/\alpha$. As for the horizontal cross-section planes $z \simeq \pm d/2$, spin textures also form square lattices whose sites sit at the plaquette centers of the former lattice. This is a body-centered cubic lattice configuration, which is a generalization of the 2D skyrmion lattice configuration in Refs. [49] into 3D. Again, if interaction is very strong to mix states in different Landau levels, the condensate will become plane-wave-like or superpositions of SO coupled plane-waves[63].

FIG. 5: From left to right: the density and phase profiles of $\psi_\uparrow(r)$ and $\psi_\downarrow(r)$ with parameter values of $\alpha = 0.5$, $\beta = 10$, $\rho = 0.97$. From (a)-(g), γ is taken as 0.5, 0.25, 0.1, 0.0, -0.1, -0.3, and -0.5, respectively. At small values of $|\gamma|$ in $[c, d,$ and $e]$, a skyrmion lattice is formed near the trap center. By increasing the magnitude of $|\gamma|$ [(b) and (f)], the skyrmion lattice evolves to the normal vortex lattice. For the large value of $|\gamma| = 0.5$ [(a) and (g)], the condensates show a lattice configuration around a ring. The black circle with an arrow indicates the direction of the circulation around the vortex core. The unit of length for the figures is l_T. From Ref. [74].

IV. VORTEX CONFIGURATIONS OF SO COUPLED BECS IN A ROTATING TRAP

Next we review the vortex configurations of SO coupled unconventional BECs in rotating traps. From a more general framework, the above-considered SO coupling can be viewed as particles subject to non-Abelian gauge fields. On the other hand, the Coriolis force from rotation behaves as an effective Abelian vector potential. Therefore, in a rotating trap, atom-laser coupling provi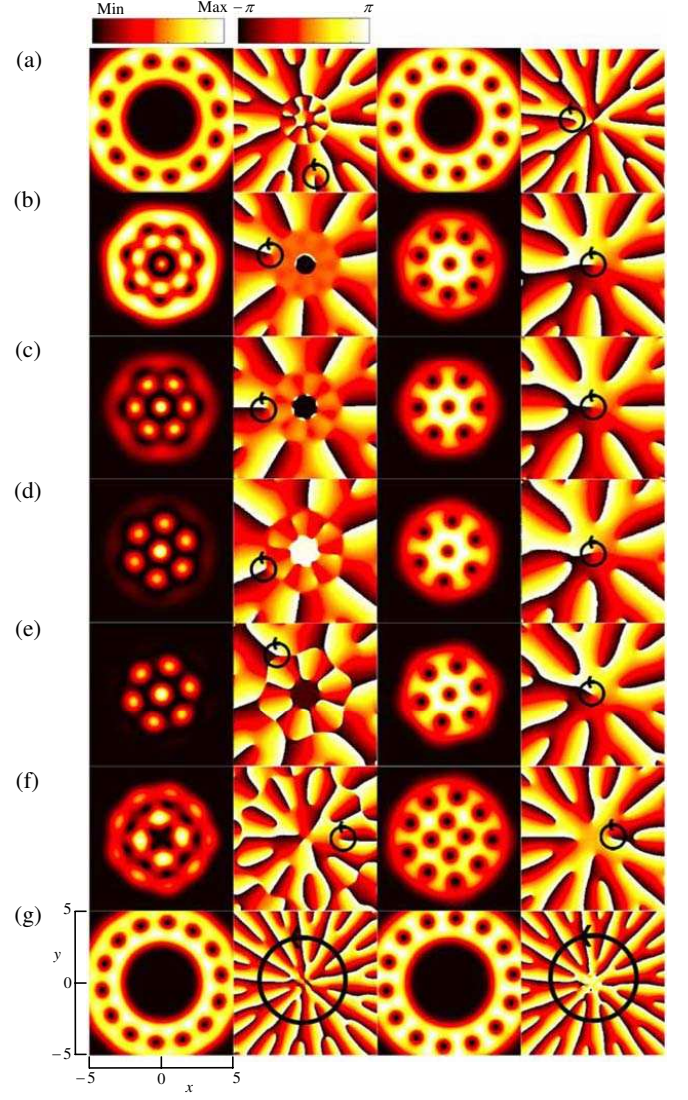des an elegant way to study the effects of these two different effective gauge fields. We only consider the rotating systems with the Rashba SO coupling.

A. Hamiltonians of SO coupled bosons in a rotating trap

Ultracold atoms in a rotating trap share similar physics of electrons subject to magnetic fields due to the similar-

ity between Lorentz and Coriolis forces. Depending on the experimental implementations of rotation, Hamiltonians can be of different types[70,71,74]. As pointed out in Ref. [70], because the current experiment setup breaks rotation symmetry, rotating SO coupled BECs is time-dependent in the rotating frame, which is a considerably more complicated problem than the usual rotating BECs. Nevertheless, below we only consider the situation of the isotropic Rashba SO coupling, such that it in principle can be implemented as a time-independent problem in the rotating frame.

The effect of rotation should be described by the standard minimal substitution method as presented in Ref. [74]. The non-interacting part of the Hamiltonian is

$$
\begin{aligned}
H_0 &= \int d^3\vec{r}\,\psi_\mu^\dagger(\vec{r})\Big[\frac{1}{2M}(-i\hbar\vec{\nabla} + M\lambda\hat{z}\times\vec{\sigma} - \vec{A})^2 - \mu \\
&+ V_{ext}(\vec{r}) - \frac{1}{2}M\Omega_z^2(x^2+y^2)\Big]_{\mu\nu}\psi_\nu(\vec{r}),
\end{aligned}
\tag{35}
$$

where the last term is the centrifugal potential due to rotation.

Note that due to the presence of SO coupling, we should carefully distinguish the difference between mechanical and canonical angular momenta. The mechanical one should be defined according to the minimal substitution as

$$
L^{mech} = L_z + M\lambda(x\sigma_x + y\sigma_y),
\tag{36}
$$

where L_z is the usual canonical angular momentum. Expanding Eq. 35, it is equivalent to Eq. 1 plus the term of angular velocity Ω_z coupling to L^{mech} as

$$
H_{rot} = -\Omega_z\int d^3\vec{r}\,\psi_\mu^\dagger(\vec{r})\Big[L^{mech}\Big]_{\mu\nu}\psi_\nu(\vec{r}).
\tag{37}
$$

Thus in the rotating frame, the effect of Ω_z is not only just $\Omega_z L_z$ as usual, but also an extra effective radial Zeeman term as

$$
\vec{B}_R(\vec{r}) = \Omega_z M\lambda\vec{r}.
\tag{38}
$$

Such a term is often missed in literatures. As will be shown below, it affects the ground state vortex configurations significantly and thus should not be overlooked.

To make the model more adjustable, an external spatially dependent Zeeman field $\vec{B}_{ex} = B\vec{r}$ is intentionally introduced as

$$
H_B = -B\int d^3r\,\psi_\mu^\dagger(\vec{r})\,(x\sigma_x + y\sigma_y)_{\mu\nu}\,\psi_\nu(\vec{r}),
\tag{39}
$$

which shares the same form as Eq. 38. Experimentally, such a Zeeman field can be generated through coupling two spin components using two standing waves in the x and y-directions with a phase difference of $\frac{\pi}{2}$. The corresponding Rabi coupling is

$$
-\Omega'\Big\{\sin(k_L x) + i\sin(k_L y)\Big\}\psi_\downarrow^\dagger(\vec{r})\psi_\uparrow(\vec{r}) + h.c.
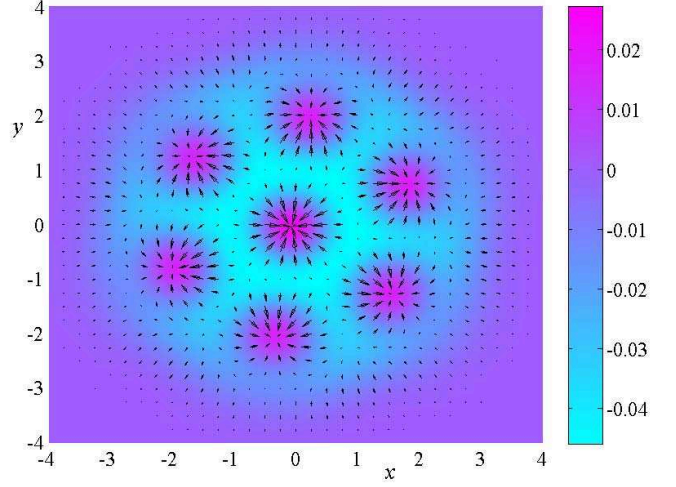\tag{40}
$$

FIG. 6: The spin density distribution of the condensate of Fig. 5 (d). The projection of $\langle\vec{\sigma}\rangle$ in the xy-plane is shown as black vectors. A color map is used to illustrate the $\langle\sigma_z\rangle$ component. The unit of length for the figure is l_T. From Ref. [74].

In the region of $|x|, |y| \ll 2\pi/k_L$, it reduces to the desired form of Eq. 39 with $B = \Omega'k_L$. Such a term compensates the non-canonical part of the mechanical momentum in H_{rot}, which renders the model adjustability in a wider range.

B. SO coupled bosons in rotating traps

Now we turn on interactions and obtain the ground state condensate numerically by solving the SO coupled GP equations which have been reduced into the dimensionless form as

$$
\begin{aligned}
\mu\tilde{\psi}_\uparrow &= \hat{T}_{\uparrow\nu}\tilde{\psi}_\nu + \beta(|\tilde{\psi}_\uparrow|^2 + |\tilde{\psi}_\downarrow|^2)\tilde{\psi}_\uparrow, \\
\mu\tilde{\psi}_\downarrow &= \hat{T}_{\downarrow\nu}\tilde{\psi}_\nu + \beta(|\tilde{\psi}_\downarrow|^2 + |\tilde{\psi}_\uparrow|^2)\tilde{\psi}_\downarrow,
\end{aligned}
\tag{41}
$$

where $(\tilde{\psi}_\uparrow, \tilde{\psi}_\downarrow)$ are normalized according to the condition $\int d\vec{r}^2(|\psi_\uparrow|^2 + |\psi_\downarrow|^2) = 1$. $\hat{T}$ is defined as

$$
\begin{aligned}
\hat{T} &= -\frac{1}{2}l_T^2(\partial_x^2 + \partial_y^2) + \alpha l_T(-i\partial_y\sigma_x + i\partial_x\sigma_y) \\
&+ \frac{1}{2l_T^2}(x^2+y^2) - \frac{\rho}{l_T}(-ix\partial_y + iy\partial_x) \\
&- \alpha\frac{\kappa}{l_T}(x\sigma_x + y\sigma_y),
\end{aligned}
\tag{42}
$$

where $\rho = \Omega_z/\omega$; $\kappa = \gamma + \rho$; and $\gamma = B/(M\omega\lambda)$ is defined for the extra radial Zeeman field in Eq. 39.

1. The skyrmion lattice structure in the weak SO coupling

Rich structures of vortex lattices appear in the case of weak SO coupling. In Fig. 5, the SO parameter is taken
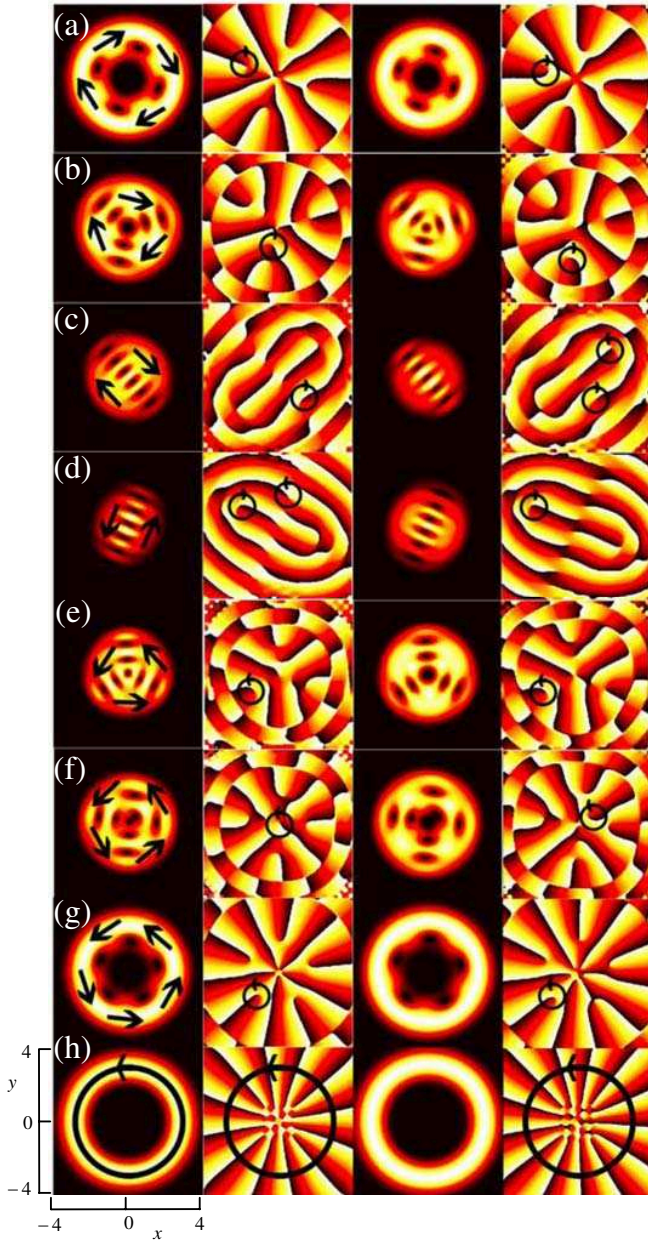
FIG. 7: From left to right: the density and phase profiles of $\psi_\uparrow(r)$ and $\psi_\downarrow(r)$ with parameter values of $\alpha = 4$, $\beta = 20$, $c = 1$, and $\rho = 0.1$. From (a)-(h), γ is taken as 0.5, 0.3, 0.1, -0.05, -0.25, -0.35, -0.6, and -0.7, respectively. The black arrow in each domain represents the local wavevector direction of the corresponding plane-wave state, which shows a clockwise or counter-clockwise configuration depending on the sign of γ. For sufficiently large values of $|\gamma|$, condensates distribute around a ring in space forming a giant vortex. The color scales for the density and phase distributions are the same as that in Fig. 5. The black circle with an arrow indicates the the direction of the circulation around the vortex core. The unit of length for the figures is l_T. From Ref. [74].

as $\alpha = 0.5$. Both the density and phase patterns for $\psi_\uparrow(r)$ and $\psi_\downarrow(r)$ are depicted. Let us first consider the case of pure rotation of $B = 0$ as shown in Fig. 5 (d), i.e., $\gamma = 0$. For $\psi_\uparrow(r)$, its density distribution exhibits several disconnected peaks. By contrast, the usual vortex lattices show disconnected low density vortex cores. The phase distribution $\psi_\uparrow(r)$ exhibits singular points around which phases wind 2π. These singular points are squeezed out to the low density region near the edge. For $\psi_\downarrow(r)$, its vortex cores are pinned by peaks of the density of $\psi_\uparrow(r)$. Combine the distributions of $\psi_\uparrow(r)$ and $\psi_\downarrow(r)$ together, the condensate exhibits a skyrmion lattice configuration with the spin distribution $\langle \vec{S} \rangle$ shown in Fig. 6.

Turning on the external Zeeman field $\vec{B}_{ex}$ of Eq. 39 changes the lattice configuration. If $\vec{B}_{ex} \parallel \vec{B}_R$, the parameter $\gamma > 0$, and otherwise $\gamma < 0$. For both $\gamma > 0$ and $\gamma < 0$, if $|\gamma|$ is small, the skyrmion lattice structures remain as depicted in Fig. 5 (b, c, e, f). Increasing $|\gamma|$ further, the condensates of both spin components are pushed outwards, and distribute around a ring with a giant vortex core, as shown in Fig. 5 (a) and (g). This ring is the location of potential minima shifted from the trap center by the H_B term. In all cases in Fig. 5 $(a$-$g)$, the difference of vortex numbers between the spin-up and down components is one. This is a characteristic feature brought by the Rashba SO coupling.

2. The domain wall structure in the strong SO coupling

As discussed in section III B, in the case of strong SO coupling, if interactions are also strong, condensates are nearly suppositions of SO coupled plane-wave states subject to the trap boundary condition. We consider the effect of rotation in this case. Limited by the numeric convergence, only a small rotation angular velocity is considered. The term of the external Zeeman field $\vec{B}_{ex}$ of Eq. 39 is also applied, which enriches the structures of the condensates as shown in Fig. 7.

The characteristic feature is that the condensate around the trap center is broken into several domains. Inside each domain, the condensate is approximated as a plane-wave state. Wavevectors are arranged such that the local spin polarizations are parallel to $\vec{B}_{ex}$ in order to minimize the Zeeman energy. At small values of $|\gamma|$ as shown in Fig. 7 $(c,$ and $d)$, a line of vortices appear at the boundary to separate two adjacent domains. Depending on the direction of $\vec{B}_{ex}$, the wavevectors inside domains can be clockwise or counterclockwise. For instance, when $\gamma > 0$, a clockwise configuration of these local wavevectors is selected in the condensate. As further increasing $|\gamma|$, different domains connect together to form a giant vortex as shown in Fig. 7 (a, g, h). Both spin components overlap with each other, and distribute around a ring with the radius of $\alpha|\gamma|l_T$. The spin textures lie along the radial direction to minimize the magnetic energy.

V. MAGNETIC PHASES OF SO COUPLED BOSONS IN OPTICAL LATTICES

It is natural to further consider the SO coupling effect in optical lattices, in particular in the Mott-insulating states[75–79]. Due to SO coupling, hopping amplitudes are spin-dependent whose values vary non-monotonically as increasing SO coupling strength. The spin-dependent hopping leads to the Dzyaloshinsky-Moriya (DM) type spin exchange models in the Mott-insulating states, which results in rich spin ordering patterns.

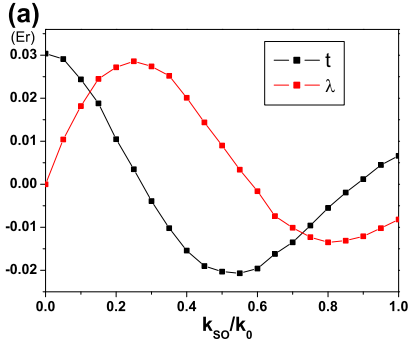### A. Tight-binding approximation and band parameters

FIG. 8: The dependence of the spin-independent hopping integral t and the spin-dependent one λ v.s. the SO coupling strength k_{so}/k_0. The optical potential depth is $V_0 = 8E_r$. From Ref. [75].

The tight-binding model in the square optical lattice will be derived below for two-component bosons with synthetic SO coupling. The single-particle Hamiltonian in the continuum is defined as in Eq. 1 by replacing the trapping potential with the periodic lattice potential as

$$V(x,y) = -V_0\Big[\cos^2 k_0 x + \cos^2 k_0 y\Big], \qquad (43)$$

where $k_0 = 2\pi/\lambda_0$ and the lattice constant $a = \lambda_0/2$. The recoil energy is defined as $E_r = \hbar^2 k_0^2/(2M)$. For later convenience, the relative strength of SO coupling is quantified by the dimensionless parameter k_{so}/k_0 with $k_{so} = M\lambda_R$.

A tight binding Hamiltonian for the lowest orbital band with SO coupling can be written as[75]

$$H = -\sum_{\langle ij\rangle,\sigma} t_{ij;\sigma\sigma'}\big[b_{i,\sigma}^\dagger b_{j,\sigma'} + h.c\big] + \sum_i [\frac{U}{2}n_i^2 - \mu n_i], \qquad (44)$$

where only the nearest neighbor hoppings are included. $t_{ij;\sigma\sigma'}$ can be decomposed into spin-independent and

spin-dependent components based on the following symmetry analysis

$$t_{ij;\sigma\sigma'} = t + i\vec{\lambda}_{ij}\cdot\vec{\sigma}. \qquad (45)$$

The coefficient of spin-dependent hopping is purely imaginary as a requirement of the TR symmetry. The optical lattice with the Rashba SO coupling possesses the reflection symmetry with respect to the vertical plane passing bonds along the x and y-directions. These reflection symmetries require that $\vec{\lambda}_{i,i+\hat{e}_x} \parallel \hat{e}_y$, and $\vec{\lambda}_{i,i+\hat{e}_y} \parallel -\hat{e}_x$. The four-fold rotation symmetry requires that $\vec{\lambda}_{i,i+\hat{e}_x}\cdot\hat{e}_y = -\vec{\lambda}_{i,i+\hat{e}_y}\cdot\hat{e}_x$. All these symmetry properties together constraint the spin-dependent hopping up to a single parameter λ as

$$\lambda_{i,i+\hat{e}_x} = \lambda\hat{e}_y, \quad \lambda_{i,i+\hat{e}_y} = -\lambda\hat{e}_x. \qquad (46)$$

The band structure parameters t and λ are related to the overlap integrals of the onsite SO coupled Wannier functions in neighboring sites. In the case of a deep lattice, each site can be approximated by a local harmonic potential. The lowest energy Wannier states $\psi_{j_z=\pm\frac{1}{2}}$ are a pair of Kramer doublets as presented in Eq. 23. The radial wavefunctions of the Wannier states $f(r)$ and $g(r)$ exhibit the Friedel-type oscillations as explained in Sec. III A. Thus naturally t and λ should also exhibit such oscillations as increasing the SO coupling parameter k_{so}/k_0. This feature is numerically confirmed using the following method. The tight-binding band spectra can be calculated easily as

$$E_\pm(\vec{k}) = \varepsilon(\vec{k}) \pm 2\lambda\sqrt{\sin^2 k_x + \sin^2 k_y}, \qquad (47)$$

where $\varepsilon(\vec{k}) = -2t(\cos k_x + \cos k_y)$. On the other hand, the band spectra can be calculated directly from the continuum model with the lattice potential Eq. 43 by using the basis of plane-waves. By fitting these spectra using Eq. 47, the values of t and λ are obtained and are plotted in Fig. 8. Both t and λ oscillate as increasing k_{so}/k_0, and the amplitudes of their overall envelops decay. For the spectra of Eq. 47, the square lattice breaks the rotational symmetry down into the 4-fold one, thus the degeneracy of the Rashba ring is lifted. The lower band has the 4-fold degenerate minima located at $\vec{Q} = (\pm k,\pm k)$ with

$$k = \tan^{-1}\frac{1}{\sqrt{2}}\frac{\lambda}{t}. \qquad (48)$$

It should be pointed out that these lowest local Wannier states are the eigenstates of the on-site total angular momentum with $j_z = \pm\frac{1}{2}$. Therefore, the eigen-bases defined by $(b_{i\uparrow}, b_{i\downarrow})^T$ should be those of j_z not σ_z. In the case of strong SO coupling $k_{so} \geq k_0$, the angular momenta of these Wannier states nearly come from the orbital angular momentum moment, while their spin moments are nearly average to zero.

If in the limit of very strong SO coupling such that $k_{so} \gg k_0$, Landau level quantization effects appear

within each site. Many states with different values of j_z are nearly degenerate as presented in Sec. II B. In this case, a single band model Eq. 44 fails even in the case of the deep lattice. It is justified only in the case that $k_{so}/k \leq 1$ in which the lowest Wannier states are separated from others.

B. Magnetic properties in the Mott-insulating state

We consider the spin physics in the Mott-insulating phase of Eq. 44. In the simplest case, there is one particle per site with a two-fold degenerate Kramer doublet. The low energy superexchange Hamiltonian can be constructed using the Schrieffer-Wolf transformation, which shows the Dzyaloshinsky-Moriya (DM) type exchange due to SO coupling[103,104] as

$$H_{eff} = \sum_i H_{i,i+\hat{e}_x} + H_{i,i+\hat{e}_y}, \tag{49}$$

and

$$
\begin{aligned}
H_{i,i+\hat{e}_\mu} &= -J_1 \vec{S}_i \cdot \vec{S}_{i+\hat{e}_\mu} - J_{12} \vec{d}_{i,i+\hat{e}_\mu} \cdot (\vec{S}_i \times \vec{S}_{i+\hat{e}_\mu}) \\
&+ J_2[\vec{S}_i \cdot \vec{S}_{i+\hat{e}_\mu} - 2(\vec{S}_i \cdot \vec{d}_{i,i+\hat{e}_\mu})(\vec{S}_{i+\hat{e}_\mu} \cdot \vec{d}_{i,i+\hat{e}_\mu})],
\end{aligned}
\tag{50}
$$

where $\hat{e}_\mu (\mu = x, y)$ are the unit vectors along the x and y-directions, respectively; $J_1 = 4t^2/U$, $J_{12} = 4t\lambda/U$, and $J_2 = 4\lambda^2/U$. The DM vectors are defined as $\vec{d}_{i,i+\hat{e}_x} = \hat{e}_y$ and $\vec{d}_{i,i+\hat{e}_y} = -\hat{e}_x$ which are perpendicular to each other. This is similar to the case of the high T_c cuprate superconductors such as $YBa_2Cu_3O_6$[105,106]. Consequently, these DM vectors in Eq. 50 cannot be removed by gauge transformations, or, equivalently by varying local spin axes. This brings frustrations to magnetic properties. To obtain a qualitative understanding, two different limits of $|\lambda| \ll |t|$ and $|\lambda| \gg |t|$ will be considered.

In the absence of SO coupling, i.e., $\lambda = 0$, the system is in the ferromagnetic state. If λ is small, the J_2-term brings the easy plane anisotropy which prefers spin moments lie in the xy-plane. The DM-vector further induces spin spiraling at a finite wavevector, which can be shown by calculating the spin-wave spectra around the variational ground states that spin moments lie along the high symmetry line of diagonal directions, say, $[1\bar{1}0]$. The Holstein-Primakoff transformation is employed to transform Eq. (49) into the magnon Hamiltonian,

$$
\begin{aligned}
H_{mg} = -J_0 \sum_i &\Big\{ (\cos 2\theta - i\frac{\sin 2\theta}{\sqrt{2}})a_i^\dagger a_{i+e_x} \\
&+ (\cos 2\theta + i\frac{\sin 2\theta}{\sqrt{2}})a_i^\dagger a_{i+e_y} + h.c \Big\},
\end{aligned}
\tag{51}
$$

where $a^\dagger$ is the creation operator for magnons deviating from the [110]-direction; $\theta = \arctan(\lambda/t)$ as defined above. We only keep quadric terms and ignore the terms

proportional to $\sin^2 \theta$ since $\lambda/t \ll 1$. In momentum space, its spectra can be diagonalized as

$$
\begin{aligned}
\epsilon(\vec{k}) = -2J_0 &\Big\{ \cos 2\theta(\cos k_x + \cos k_y) \\
&+ \frac{1}{\sqrt{2}} \sin 2\theta(\sin k_x - \sin k_y) \Big\},
\end{aligned}
\tag{52}
$$

whose minima are located at $\vec{Q}_M = (2k, -2k)$ with the value of k given in Eq. 48. This indicates that the ground state exhibits a spin spiral order along the direction perpendicular to the quantized axis in the spin-wave analysis.

Interestingly, in the opposite limit of $|\lambda/t| \gg 1$, Eq. 50 can be related to that of $|\lambda/t| \ll 1$ through a duality transformation. On site i with the coordinates (i_x, i_y), $\vec{S}_i$ is transformed into

$$
\begin{aligned}
S_{i_x,i_y}^x &\to (-1)^{i_x} \mathbb{S}_{i_x,i_y}^x; \quad S_{i_x,i_y}^y \to (-1)^{i_y} \mathbb{S}_{i_x,i_y}^y; \\
S_{i_x,i_y}^z &\to (-1)^{i_x+i_y} \mathbb{S}_{i_x,i_y}^z.
\end{aligned}
\tag{53}
$$

$\mathbb{S}_i$ still maintains the spin commutation relation. Under this transformation, the J_1-term transforms into the J_2-term and vice versa, and the J_{12}-term is invariant. Thus this dual transformation indicates that there is a one-to-one correspondence between the J_2-dominant phase ($|\lambda/t| \gg 1$) and that of J_1 with $|\lambda/t| \ll 1$ which has been analyzed above.

In the regime of intermediate values λ/t, a rich phase diagram with different spin patterns appears. Classical Monte Carlo simulations have been employed to calculate the ground state phase diagram in current literatures[76–78]. Various patterns have been found as a result of competition among ferromagnetic exchange, easy-plane anisotropy, and the DM effect induced spin spirals. These include the ferromagnetic, antiferromagnetic, spiral, stripes, and vortex crystal orderings. Furthermore, the superfluid-insulator transition for SO coupled bosons has also been studied in Ref. [79].

VI. CONCLUSIONS

We have reviewed unconventional BECs with SO coupling whose condensate wavefunctions are complex-valued and are thus beyond the framework of the "no-node" theorem. Even at the single particle level, the spectra in harmonic traps exhibit the structure of Landau-level like quantization induced by SO couplings. Their energy dispersion is nearly flat with respect to angular momentum in the case of strong SO coupling, and exhibit the Z_2-type topology. The interacting condensates exhibit topologically non-trivial configurations. In the 2D Rashba case, the spin density distributions are characterized by the skyrmion type textures. The 3D Weyl SO coupling induces the topological phase defects in the quaternionic phase space, and the corresponding spin density distributions are also non-trivial carrying non-zero values of the Hopf-invariant. In rotating traps, the

condensate configurations are changed by vorticity which results in a variety of structures including skyrmion lattices, giant vortices, multi-domains of plane-waves. In the strongly correlated Mott-insulating states, SO coupling exhibits in the DM exchange interactions in the quantum magnetism. The research of the novel states of SO coupled bosons is still in the early stage. In particular, the effect of SO couplings in the strong correlation regime is still a largely unexplored field. We expect that further exciting progress on the novel states of SO coupled bosons will appear in the near future.

Acknowledgments

[1] I. Žutić, J. Fabian, and S. Das Sarma, Rev. Mod. Phys. **76**, 323 (2004).

[2] N. Nagaosa *et al.*, Rev. Mod. Phys. **82**, 1539 (2010).

[3] D. Xiao, M.-C. Chang, and Q. Niu, Reviews of Modern Physics **82**, 1959 (2010).

[4] M. D'yakonov and V. Perel, Soviet Journal of Experimental and Theoretical Physics Letters **13**, 467 (1971).

[5] J. E. Hirsch, Phys. Rev. Lett. **83**, 1834 (1999).

[6] S. Murakami, N. Nagaosa, and S.-C. Zhang, Science **301**, 1348 (2003).

[7] J. Sinova *et al.*, Physical Review Letters **92**, 126603 (2004).

[8] M. Z. Hasan and C. L. Kane, Rev. Mod. Phys. **82**, 3045 (2010).

[9] X.-L. Qi and S.-C. Zhang, Rev. Mod. Phys. **83**, 1057 (2011).

[10] Y. Lin *et al.*, Nature **462**, 628 (2009).

[11] Y. Lin *et al.*, Phys. Rev. Lett. **102**, 130401 (2009).

[12] Y. Lin, K. Jimenez-Garcia, and I. Spielman, Nature **471**, 83 (2011).

[13] J. Zhang *et al.*, Phys. Rev. Lett. **109**, 115301 (2012).

[14] P. Wang *et al.*, Phys. Rev. Lett. **109**, 095301 (2012).

[15] C. Qu *et al.*, arXiv:1301.0658 (2013).

[16] L. W. Cheuk *et al.*, Physical Review Letters **109**, 095302 (2012).

[17] R. P. Feynman, *Statistical Mechanics, A Set of Lectures* (Addison-Wesley Publishing Company, ADDRESS, 1972).

[18] C. Wu, Mod. Phys. Lett. B **23**, 1 (2009).

[19] A. Isacsson and S. M. Girvin, Phys. Rev. A **72**, 053604 (2005).

[20] W. V. Liu and C. Wu, Phys. Rev. A **74**, 013607 (2006).

[21] A. B. Kuklov, Phys. Rev. Lett. **97**, 110405 (2006).

[22] Z. Cai and C. Wu, Phys. Rev. A **84**, 033635 (2011).

[23] T. Müller, S. Fölling, A. Widera, and I. Bloch, Phys. Rev. Lett. **99**, 200405 (2007).

[24] G. Wirth, M. Ölschläger, and A. Hemmerich, Nature Physics **7**, 147 (2010).

[25] M. Ölschläger, G. Wirth, and A. Hemmerich, Phys. Rev. Lett. **106**, 015302 (2011).

[26] C. Wu, I. Mondragon-Shem, arXiv:0809.3532V1; C. Wu, I. Mondragon-Shem, and X.-F. Zhou, Chin. Phys. Lett. **28**, 097102 (2011).

[27] T. D. Stanescu, B. Anderson, and V. Galitski, Phys. Rev. A **78**, 023616 (2008).

[28] J. Ruseckas, G. Juzeliūnas, P. Öhberg, and M. Fleischhauer, Phys. Rev. Lett. **95**, 010404 (2005).

[29] K. Osterloh *et al.*, Phys. Rev. Lett. **95**, 010403 (2005).

[30] D. L. Campbell, G. Juzeliūnas, and I. B. Spielman, Phys. Rev. A **84**, 025602 (2011).

[31] G. Juzeliunas, J. Ruseckas, D. Campbell, and I. Spielman, in *SPIE OPTO*, International Society for Optics and Photonics (PUBLISHER, ADDRESS, 2011), pp. 79500M–79500M.

[32] J. Dalibard, F. Gerbier, G. Juzeliūnas, and P. Öhberg, Rev. Mod. Phys. **83**, 1523 (2011).

[33] C. Wang, C. Gao, C. Jian, and H. Zhai, Phys. Rev. Lett. **105**, 160403 (2010).

[34] T. Ho and S. Zhang, Phys. Rev. Lett. **107**, 150403 (2011).

[35] B. Anderson, J. Taylor, and V. Galitski, Phys. Rev. A **83**, 031602 (2011).

[36] M. Burrello and A. Trombettoni, Phys. Rev. A **84**, 043625 (2011).

[37] T. Kawakami, T. Mizushima, and K. Machida, Phys. Rev. A **84**, 011607 (2011).

[38] Y. Li and C. Wu, arXiv:1103.5422 (2011).

[39] S. Sinha, R. Nath, and L. Santos, Phys. Rev. Lett. **107**, 270401 (2011).

[40] Z. F. Xu, R. Lü, and L. You, Phys. Rev. A **83**, 053602 (2011).

[41] S.-K. Yip, Phys. Rev. A **83**, 043616 (2011).

[42] Q. Zhu, C. Zhang, and B. Wu, arXiv:1109.5811 (2011).

[43] B. Anderson and C. Clark, arXiv:1206.0018 (2012).

[44] B. M. Anderson, G. Juzeliūnas, V. M. Galitski, and I. B. Spielman, Phys. Rev. Lett. **108**, 235301 (2012).

[45] R. Barnett *et al.*, Phys. Rev. A **85**, 023615 (2012).

[46] Y. Deng *et al.*, Phys. Rev. Lett. **108**, 125301 (2012).

[47] T. Grass, B. Juliá-Díaz, and M. Lewenstein, arXiv:1210.8035 (2012).

[48] P. He, R. Liao, and W. Liu, Phys. Rev. A **86**, 043632

(2012).

[49] H. Hu, B. Ramachandhran, H. Pu, and X. Liu, Phys. Rev. Lett. **108**, 10402 (2012).

[50] Y. Li, L. Pitaevskii, and S. Stringari, Phys. Rev. Lett. **108**, 225301 (2012).

[51] B. Ramachandhran *et al.*, Phys. Rev. A **85**, 023606 (2012).

[52] E. Ruokokoski, J. Huhtamäki, and M. Möttönen, arXiv:1205.4601 (2012).

[53] T. Sedrakyan, A. Kamenev, and L. Glazman, arXiv:1208.6266 (2012).

[54] X. Xu and J. Han, Phys. Rev. Lett. **108**, 185301 (2012).

[55] Z. Xu, Y. Kawaguchi, L. You, and M. Ueda, Phys. Rev. A **86**, 033628 (2012).

[56] D. Zhang, L. Fu, Z. Wang, and S. Zhu, Phys. Rev. A **85**, 043609 (2012).

[57] X. Zhang *et al.*, Phys. Rev. A **86**, 063628 (2012).

[58] Y. Zhang, L. Mao, and C. Zhang, Phys. Rev. Lett. **108**, 35302 (2012).

[59] W. Zheng and Z. Li, Phys. Rev. A **85**, 053607 (2012).

[60] X. Cui and Q. Zhou, arXiv:1206.5918 (2012).

[61] Y. Li, X. Zhou, and C. Wu, Phys. Rev. B **85**, 125122 (2012).

[62] H. Weyl, Z. Phys. **56**, 330 (1929).

[63] Y. Li, X. Zhou, and C. Wu, arXiv:1205.2162 (2012).

[64] T. Kawakami, T. Mizushima, M. Nitta, and K. Machida, Phys. Rev. Lett. **109**, 015301 (2012).

[65] D.-W. Zhang *et al.*, arXiv:1301.2869 (2013).

[66] W. Yao and Q. Niu, Physical Review Letters **101**, 106401 (2008).

[67] A. High *et al.*, arXiv:1103.0321 (2011).

[68] A. High *et al.*, Nature (2012).

[69] S. K. Ghosh, J. P. Vyasanakere, and V. B. Shenoy, Phys. Rev. A **84**, 053629 (2011).

[70] J. Radić, T. Sedrakyan, I. Spielman, and V. Galitski, Phys. Rev. A **84**, 063604 (2011).

[71] X. Xu and J. Han, Phys. Rev. Lett. **107**, 200401 (2011).

[72] C. Liu and W. Liu, Phys. Rev. A **86**, 033602 (2012).

[73] Y. Zhao, J. An, and C. Gong, Phys. Rev. A **87**, 013605 (2013).

[74] X. Zhou, J. Zhou, and C. Wu, Phys. Rev. A **84**, 063624 (2011).

[75] Z. Cai, X. Zhou, and C. Wu, Phys. Rev. A **85**, 061605 (2012).

[76] W. Cole, S. Zhang, A. Paramekanti, and N. Trivedi, Phys. Rev. Lett. **109**, 85302 (2012).

[77] J. Radić, A. Di Ciolo, K. Sun, and V. Galitski, Phys. Rev. Lett. **109**, 85303 (2012).

[78] M. Gong, Y. Qian, V. Scarola, and C. Zhang, arXiv preprint arXiv:1205.6211 (2012).

[79] S. Mandal, K. Saha, and K. Sengupta, arXiv preprint arXiv:1205.3178 (2012).

[80] M. Iskin and A. Subaşı, Phys. Rev. Lett. **107**, 50402 (2011).

[81] L. Jiang, X. Liu, H. Hu, and H. Pu, Phys. Rev. A **84**, 063618 (2011).

[82] J. Zhou, W. Zhang, and W. Yi, Phys. Rev. A **84**, 063603 (2011).

[83] E. Doko, A. Subaşı, and M. Iskin, Phys. Rev. A **85**, 053634 (2012).

[84] L. He and X. Huang, Phys. Rev. Lett. **108**, 145302 (2012).

[85] L. He and X. Huang, arXiv:1207.2810 (2012).

[86] H. Hu *et al.*, arXiv:1208.5841 (2012).

[87] X. Liu, Phys. Rev. A **86**, 033613 (2012).

[88] D. Maldonado-Mundo, P. Ohberg, and M. Valiente, arXiv:1212.3565 (2012).

[89] G. Martone, Y. Li, L. Pitaevskii, and S. Stringari, Phys. Rev. A **86**, 063621 (2012).

[90] P. Orth *et al.*, arXiv:1212.5607 (2012).

[91] J. Vyasanakere and V. Shenoy, arXiv:1201.5332 (2012).

[92] S. Zhang, X. Yu, J. Ye, and W. Liu, arXiv:1212.0424 (2012).

[93] Y. Li, S.-C. Zhang, and C. Wu, arXiv:1208.1562 (2012).

[94] Y. Li, K. Intriligator, Y. Yu, and C. Wu, Phys. Rev. B **85**, 085132 (2012).

[95] B. I. Halperin, Phys. Rev. B **25**, 2185 (1982).

[96] F. Zhou, International Journal of Modern Physics B **17**, 2643 (2003).

[97] B. Ramachandhran, H. Hu, and H. Pu, arXiv:1301.0800 (2013).

[98] S. Adler, *Quaternionic quantum mechanics and quantum fields* (Oxford University Press, USA, ADDRESS, 1995), Vol. 88.

[99] D. Finkelstein, J. Jauch, S. Schiminovich, and D. Speiser, Journal of mathematical physics **3**, 207 (1962).

[100] A. Balatsky, arXiv preprint cond-mat/9205006 (1992).

[101] F. Wilczek and A. Zee, Phys. Rev. Lett. **51**, 2250 (1983).

[102] M. Nakahara, *Geometry, topology and physics* (Taylor & Francis, ADDRESS, 2003).

[103] I. Dzyaloshinsky, Journal of Physics and Chemistry of Solids **4**, 241 (1958).

[104] T. Moriya, Phys. Rev. **120**, 91 (1960).

[105] D. Coffey, T. M. Rice, and F. C. Zhang, Phys. Rev. B **44**, 10112 (1991).

[106] N. E. Bonesteel, Phys. Rev. B **47**, 11302 (1993).